Applied Surface Science 589 (2022) 152902

Contents lists available at ScienceDirect

Applied Surface Science

journal homepage: www.elsevier.com/locate/apsusc

Full Length Article

Degradation of tetracycline hydrochloride (TCH) by active photocatalyst rich in oxygen vacancies: Performance, transformation product and mechanism

Liwei Wang [a,b,c], Anjie Hu [a], Hongjie Liu [b,d], Kefu Yu [a,c,*], Shaopeng Wang [a,c], Xianwang Deng [a], Dahua Huang [a]

[a] School of Marine Sciences, Coral Reef Research Center of China, Guangxi Laboratory on the Study of Coral Reefs in the South China Sea, Guangxi University, Nanning 530004, PR China
[b] School of Resources, Environment and Materials, Guangxi Key Laboratory of Processing for Non-ferrous Metallic and Featured Materials, Guangxi University, Nanning 530004, PR China
[c] Southern Marine Science and Engineering Guangdong Laboratory (Zhuhai), Zhuhai 519080, PR China
[d] School of Chemistry and Chemical Engineering, Guangxi University, Nanning 530004, PR China

ARTICLE INFO

Keywords:
Oxygen vacancy
BiOBr microsphere
Solvent coordination
Self-assembly
Photodegradation
Tetracycline hydrochloride

ABSTRACT

Regulation of oxygen defects, in addition to the adjustment of spatial arrangement and bandgap in the materials can effectively improve the materials' photocatalytic performance. Bismuth oxybromide (BiOBr) are widely used in the field of photocatalysis because of its abundant active sites and the regulable surface area. Herein, a novel introducing oxygen vacancies (OVs) strategy was developed to synthesize hierarchical 3D BiOBr microsphere constructed by nanopetals, and a serious of tests were used to characterize and quantify OVs. Moreover, the applications of BiOBr with different concentrations of OVs in water antibiotic pollution was discussed, and specific effect of OVs on the photocatalytic performance was also analyzed simply. Benefiting from its rich OVs, the UV–*vis* light-driving tetracycline hydrochloride degradation efficiency increased to 86.8% within 20 min irradiation. Hence, this work provides theoretical guidance for the regulation of OVs, and the prospect of photocatalyst containing OVs in the photocatalytic field were suggested.

1. Introduction

The accumulation of antibiotics in surface water basins stems from the frequent use of drugs and aquaculture, thus leading to the evolution of drug-resistant strains and environmental contamination. Nowadays, compared to other techniques [1–4], semiconductor-based photocatalytic degradation is considered as a safe, quick, low energy consumption and repeatable strategy for reducing environmental and energy crises using solar energy [5–7]. Therefore, it is worthwhile to explore the novel semiconductor-based photocatalyst to boost this technology. Furthermore, the presence of structure defect can help narrow the band gap of the photocatalyst to improve the degradation efficiency [8–12].

Oxygen vacancies (OVs), one of the nonstoichiometric defects, have been attracting massive attention in improving the material properties based on it can behave as important adsorption and active sites for catalysis [13]. Especially, introducing OVs on the catalyst surface has been considered a facile, effective and prevalent method to strongly influence the reactivity of catalytic performances [14,15]. It has been shown that the photocatalytic properties including the electronic structure [16], charge transport, and surface properties of catalyst are closely related to OVs [17]. In addition, the formation of OVs on the surface introduce more unpaired electrons or highly reactive and unsaturated dangling bonds, which could provide potential active sites to facilitate the catalytic reactions [18]. Moreover, OVs have significant influences on affecting the e^{-}-h^{+} recombination process in photocatalysts, capturing the photogenerated electrons, and facilitate the surface adsorption of substrate molecules [19]. For instance, the recent relevant reported. reported the photocatalysts with abundant OVs to help effectively photodegrade the water pollutions [20–22]. Hence, it is

* Corresponding author at: School of Marine Sciences, Coral Reef Research Center of China, Guangxi Laboratory on the Study of Coral Reefs in the South China Sea, Guangxi University, Nanning 530004, PR China.
E-mail address: kefuyu@scsio.ac.cn (K. Yu).

https://doi.org/10.1016/j.apsusc.2022.152902
Received 29 November 2021; Received in revised form 12 February 2022; Accepted 20 February 2022
Available online 26 February 2022

an urgent task to adjust the OVs concentrations for the significant improvement of the optical and electronic properties in photocatalysts.

Recently, bismuth oxybromide (BiOBr) has attracted increasing attention due to its stability, and processing into multi-dimensional superstructures with lamellar nanounits [23–25]. Therefore, a novel solvent-coordination induced self-assembly solvothermal strategy was developed to synthesize hierarchical 3D BiOBr microsphere (denoted as sample S1) constructed by large numbers of ultra-thin nanoplates (thickness of ~7.5 nm), where EG played as both complexant and cross linker due to its stretching hydroxyl groups and high permittivity. And more importantly, OVs could be created when EG were removed, thus decreasing the recombination rates of e^{-}-h^{+} pairs for photocatalysis [26,27]. For comparison, several other solvents with different polarities (isopropanol, ethanol, tetrahydrofuran and water) were also used to generate BiOBr counterparts under the same conditions, labelled as sample S2-S5, respectively. Benefiting from the rich amount of OVs in sample S1, the UV–*vis* light-driving tetracycline hydrochloride (TCH) degradation efficiency increased to 86.8% within 20 min radiation, 10.7–30.1% higher than those for other four samples. Combining a series of tests and theoretical calculations, it can be concluded that richer OVs can promote the electron transfer and surface adsorption in the TCH photodegradation. In summary, this work displays a rational regulation of OVs upon the BiOBr microsphere, thus obtaining the excellent photodegradation performances, and promising actual light-driven purification technology.

2. Experimental section

2.1. Synthesis of BiOBr microsphere

BiOBr powder was synthesized by a simple solvothermal method. In a typical synthesis, 1 mmol of $Bi(NO_3)_3{\cdot}5H_2O$ and 400 mg of PVP were dissolved in five solutions (30 mL for each) with different coordination capabilities (ethylene glycol, isopropanol, ethanol, tetrahydrofuran and water). After rapid stirring for 30 min, 1 mmol of NaBr was added to the solution and continued stirring for 1.0 h at room temperature. Afterwards, the mixture was poured into a 50 mL Teflon-lined stainless steel autoclave, which was heated at 160 °C for 3 h and then cooled to room temperature. The product was washed several times with deionized water and ethanol to remove unreacted chemicals and solvents. Finally, it was dried overnight in a vacuum oven at 60 °C. The products obtained from different solvents were labelled as sample S1 to S5, respectively.

2.2. Photocatalyst characterization

The samples were characterized by means of powder XRD analysis (Rigaku Ultima IV, Cu Kα radiation, λ = 1.5418 Å, Japan), Field-emission SEM (Hitachi SU5000, Japan), TEM and HRTEM with EDS (FEI TeN-Cai G2 f20 s-twin, 200 kV, USA), HADDF-STEM (JEM-ARM200F Japan)AFM (Hitachi 5100 N Japan), XPS (Thermo SCIENTIFIC ESCALAB 250Xi, Al Kα X-ray monochromator, USA), Electron paramagnetic resonance (EPR) spectra (Bruker A300, Germany), Steady state and transient state fluorescence spectrometer (HORIBA TCSPC FluoroLog^{-3}, USA), Time-resolved PL (TR-PL) spectra (FLSP-980 Edinburgh, UK), UV/Vis/NIR spectrophotometer (PerkinElmer, LAMBDA 1050+, USA), the surface photovoltage spectroscopy (SPV) measurement (CEL-SPS1000, China), the transient photovoltage spectroscopy (TPV) measurements (CEL-TPV2000, China), BET (Autosorb-IQ, USA), Raman spectroscopy (Renishaw inVia, UK), TG-FTIR (TGA 8000-FT-IR, PerkinElmer, USA). Respectively, for probing of $^{\bullet}O_2^{-}$ and $^{\bullet}OH$ radical, 5,5-dimethyl-1-pyrroline-N-oxide (DMPO) and catalysts were dissolved in a methanol or aqueous solution, then placed the mixed solution into a paramagnetic tube and irradiated with Xe lamp to test. Total Organic Carbon (TOC) analyzer (Shimadzu, TOC-L CPH, Japan).

2.3. Photodegradation of tetracycline hydrochloride

Evaluation of the photocatalytic activities of the obtained BiOBr samples were performed by the degradation of TCH under UV–*vis* light, visible light and actual sunlight irradiation, respectively.

Firstly, 20 mg L^{-1} of TCH solution was prepared and stored in refrigerator for subsequent use. The photocatalyst powder (20 mg) obtained from **Part 2.1** was added into 100 mL of TCH solution in quartz tube and an UV–*vis* light was used by a 350 W Xenon lamp (CEL-PF300-T8E, 300–780 nm, China). Before the photocatalytic degradation, the mixtures in quartz container were stirred for 30 min in darkness in order to attain an absorption–desorption equilibrium between the powder and solution. The average light intensity of the lamp was about 886 mW cm^{-2} as measured by a light power meter (CEL-NP2000-10, China).

Secondly, the sample extraction process can be divided into two steps. During the initial 10 min, 4 mL of the suspensions were extracted every 2 min; then every 10 min for the residual 50 min. All the groups were then filtered through a 0.22 μm of PTFE syringe to obtain the supernatant solutions. The residual TCH concentrations were measured by testing the absorbance of as-obtained supernatant solutions through the UV–*vis* spectra (SHIMADZU UV-2700 spectrophotometer), and the test absorbance wavelength was chosen as 356 nm according to the optimal absorption peak of TCH solution. Besides, we also compared the UV–*vis* adsorption results with other common international methods such as HPLC testing, which can be seen in the supporting information.

In addition, the photodegradation processes under visible light (5 W Xe lamp, PCX50B 400–780 nm, China) and actual sunlight irradiation were similar to that under UV–*vis* light, and the average light intensities for them were about 35.4 mW cm^{-2} and 54.0 mW cm^{-2}.

2.4. Identification of degradation products

The photocatalytic degradation products in the solutions were determined by Thermo Fisher Ultra performance liquid chromatography/tandem mass spectrometry (UPLC-MS/MS) system, and the detailed compounds during each process can be seen in the **Fig. S16** of the supporting information.

3. Results and discussion

3.1. Structure and morphology

The phases and crystallographic structure of the samples were investigated through XRD characterization. As shown in Fig. 1a, the XRD patterns of various BiOBr products show that all the resolved diffraction peaks are well indexed to pure tetragonal phase (JCPDS No. 09-0393) but without characteristic peaks of other compounds [28], indicating the high purity of the five prepared BiOBr catalysts. Especially, the sharp diffraction peaks of sample S1 show that the good coordination ability of EG is beneficial to the orderly assembly and gradual growth of grains, leading to the construction of BiOBr photocatalyst with well crystallinity.

Furthermore, the typical high-magnified FESEM images of sample S1 (Fig. 1b and c) present the hierarchical 3D microspheres with the assistance of EG solvent, tightly assembled by interwoven ultra-thin nanoplates with average size of approximately 1.8 μm. Contrarily, rough, nonuniform and group-shaped structures can be observed with other four solvents in Fig. S1a-h, including some irregular spheres and blocks with different sizes. The TEM results in Fig. 1d and Fig. S2 further reveal more detailed morphological information about sample S1, where the clear contrast and wrinkled edges prove the ultra-thin nanounits of microsphere again. Besides, the clear lattice stripe of HRTEM image (Fig. 1e) further indicates the good crystallization of sample S1, and the planar lattice spacing of 0.277 nm corresponds to its (1 1 0) plane. While the corresponding SAED plot (Fig. 1f) indicates that the sample is polycrystalline in micro-structure. As presented in HAADF-STEM image

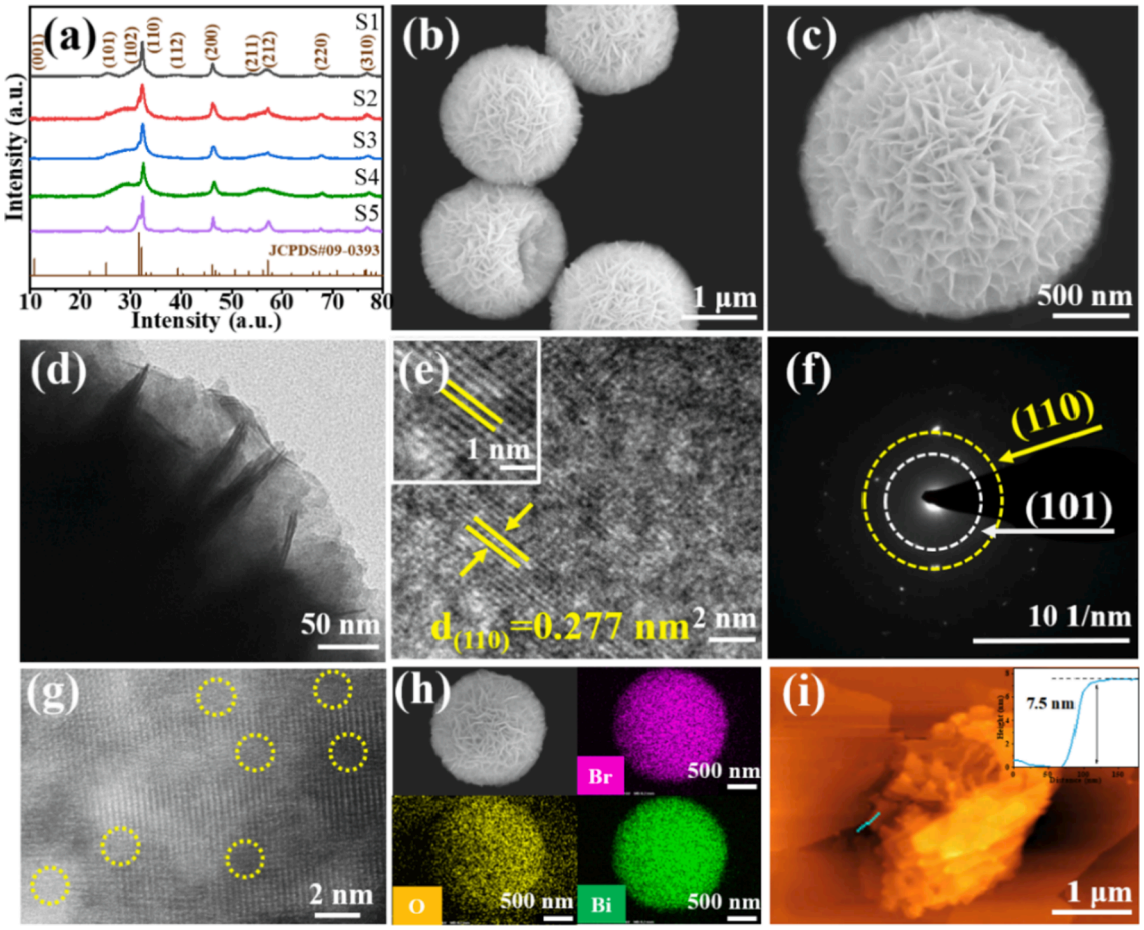

Fig. 1. (a) The XRD patterns of all the as-prepared BiOBr samples, (b-c) SEM images, (d) TEM image, (e) HRTEM image, (f) SAED pattern, (g) HAADF-STEM image, (h) mapping images, (i) AFM image and the corresponding height profiles of sample S1.

(Fig. 1g), clear lattice disorder and dislocations have been observed in sample S1, highlighting the proof of the existence of numerous OVs defects. Besides, the elemental mapping and EDS analysis (Fig. 1h and Fig. S3) confirm the presence and uniform distribution of Bi, O and Br element in the sample S1. Lastly, the thickness of the nanoplates was further measured by AFM test (Fig. 1i) with 7.5 nm, and the results are consistent with the conclusion in Fig. 1d.

To further understand the structural characteristics of the photocatalysts, nitrogen adsorption-desorption was analyzed in Fig. S4 of the supporting information. As can be seen, the specific surface areas were calculated by BET method and the corresponding BJH pore size distributions shown in Table S1, In general, the largest surface area and relatively moderate pore size of sample S1 (57.7176 m^2 g^{-1}, 4.31 nm) are favorable for efficient antibiotic adsorption.

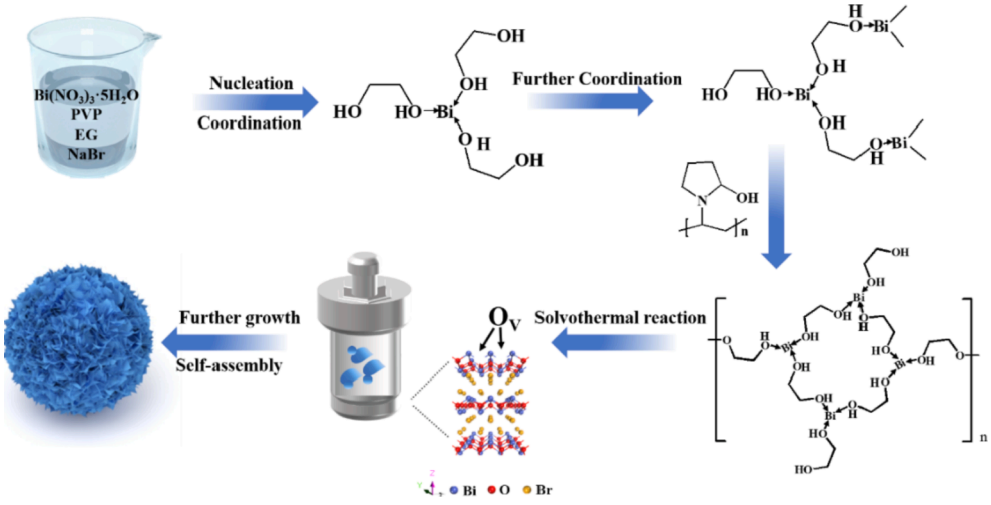

Fig. 2. The schematic illustration for the proposed regulation process of OVs in sample S1 (EG as complexant and cross-linker).

3.2. Proposed formation process of hierarchical 3D microspheres (sample S1)

Previous work reported that EG played both the roles as a complexant and cross-linker in fabricating metal oxides with different concentrations of OVs due to its high permittivity and viscosity [29,30]. Hence, EG was introduced as an excellent reaction medium for the regulation of OVs in BiOBr photocatalysts. Fig. 2 presents a plausible regulation process of OVs for the formation of hierarchical 3D microspheres (sample S1) in EG solvent. Firstly, the initial nuclei are generated by the coordination of EG and Bi^{3+} ions as the form of Bi ← OH coordination bonds. Then the side chain from the nuclear center extends along with the PVP template while coordinating with more Bi^{3+} ions, leading to the prolonging and spatial intertwining of the branched chains, forming the embryonic form of nanoplate assembly units. Subsequently, BiO^{+} ions are gradually produced because the complexes would be weakened at a relatively high temperature and an automatically generated vapor pressure under solvothermal treatment [31]. As the temperature of the reaction system increases, Br^{-} ions can directly insert into BiO^{+} ions layers to form the nanoplates of the target compound BiOBr [32]. Followingly, these nanoplates tend to bind to each other to reduce the total surface energy under solvothermal treatment inserted and OVs can be created when EG is removed [31]. Finally, the hierarchical 3D BiOBr with a tunable concentration of OVs can be obtained due to the different permittivity and viscosity of various solutions.

3.3. Electrical and optical property measurements

As far as we know, some advanced characterization techniques can not only detect the existence of OVs at both qualitative and semi-quantitative scale, but also help explain the role of OVs in catalytic materials, such as Scanning Tunneling Microscopy [33], X-ray Photoelectron Spectroscopy [34,35], Electron paramagnetic resonance (EPR) [10,36], and so on. Hence, in this work, the above techniques were used to characterize OVs combined with DFT calculations. The analysis of these characterizations is as follows:

The surface compositions and chemical valence states of the samples S1-S5 were investigated by XPS analysis. The binding energies determined from the XPS were corrected for specimen charging by internally referencing C 1s line to 284.6 eV. The XPS spectrum in Fig. S5a shows that all the BiOBr products are composed of three elements of Br, O and Bi. In the high-resolution spectrum of S5b, two strong peaks at 158.1 eV and 163.4 eV could be assigned to the binding energies of Bi $4f_{7/2}$ and Bi $4f_{5/2}$, respectively, which is characteristic to Bi^{3+} in BiOBr [37]. As for the high-resolution XPS spectrum of the Br 3d (Fig. S5c), 68.2 eV and 69.1 eV are consistent with the binding energies of Br $3d_{5/2}$ and Br $3d_{3/2}$, respectively, indicating the existence of the Br^{-} anions [23]. Meanwhile, as shown in Fig. 3a, the O 1s peak could be fitted by three peaks centered at ~528.6, 529.2 and 530.2 eV, confirming the existence of three different chemical states of oxygen species, namely lattice oxygen (O_1) belonging to the Bi-O bonds and Br-O bonds, oxygen vacancy (O_2) and chemisorbed oxygen (O_3) like –OH [35]. Correspondingly, Table S2 summarizes the relative percentages of three oxygen species on the surface of five samples, respectively. Obviously, the relatively higher OVs content in the oxygen chemical state can be seen in the sample S1, implying its stronger photocatalytic degradation potential. Interestingly, as shown in Fig. 4a, sample S1 did display the optimal photocatalytic degradation activity, consisting with the XPS conclusions.

Besides, EPR spectroscopy is known to be a sensitive and effective method for examining unpaired electrons in the materials to verify the existence of OV. In the EPR spectrum (Fig. 3b), the obvious EPR signal at about g = 2.003 can be seen obviously in all the BiOBr samples, indicating the electron trapping at OV sites [36]. Remarkably, the signal intensity in sample S1 is strongest, and the amount of surface OVs in sample S1 is higher than those in the other four catalysts, which can be attributed to the removing of EG from the coordination assembly precursor during the solvothermal treatment, when the structure of Bi ← EtOH bond will be destroyed to form these high-energy reaction sites OVs [26,27].

As is known, Raman spectroscopy is a useful tool for the identification of microstructural changes. As shown in Fig. S5d, the Raman bands at around 113 cm^{-1} and 163 cm^{-1} can be assigned to the internal A_{1g} Bi-Br stretching modes and the E_{1g} internal Bi-Br stretching modes [38]. Notably, the bands that appeared at 91 cm^{-1} can be assigned to the A1g first-order vibration modes of the Bi metal, which is due to the formation of OVs in samples S1-5 [39]. And compared with samples S2-5, the peak

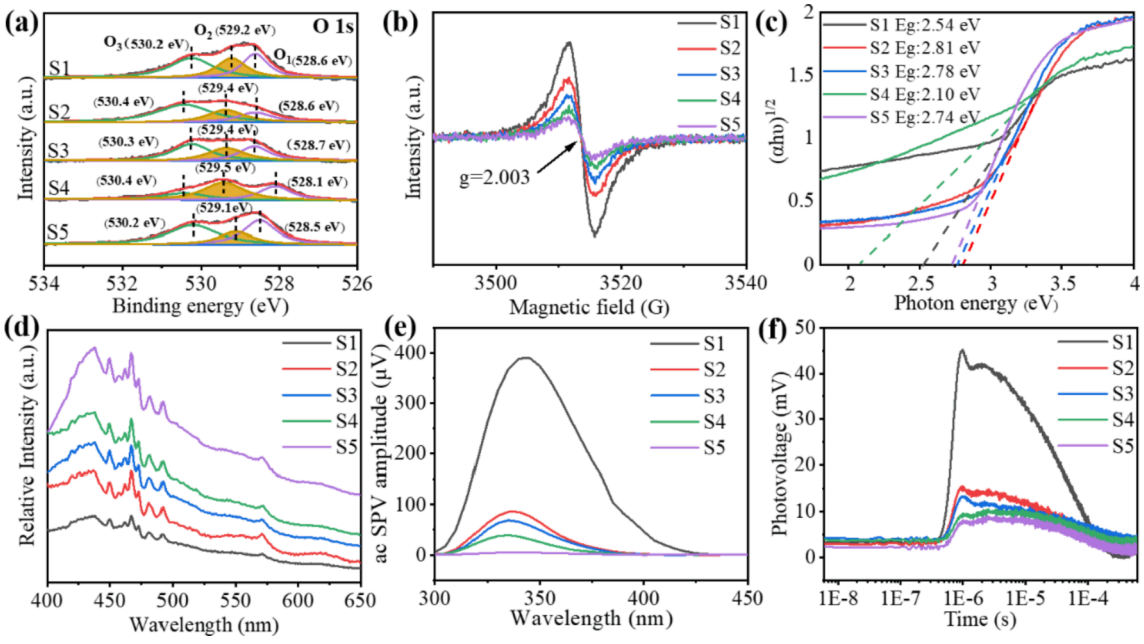

Fig. 3. Surfaces state characterizations of S1-S5: (a) High-resolution XPS spectra of O 1s, (b) EPR spectra, (c) the energy gap calculated by plotting $(\alpha h\nu)^{1/2}$ versus $h\nu$, (d) emission PL spectra with excitation wavelength at 325 nm at room temperature, (e) SPV spectra and (f) TPV responses excited by the laser pulse at 355 nm.

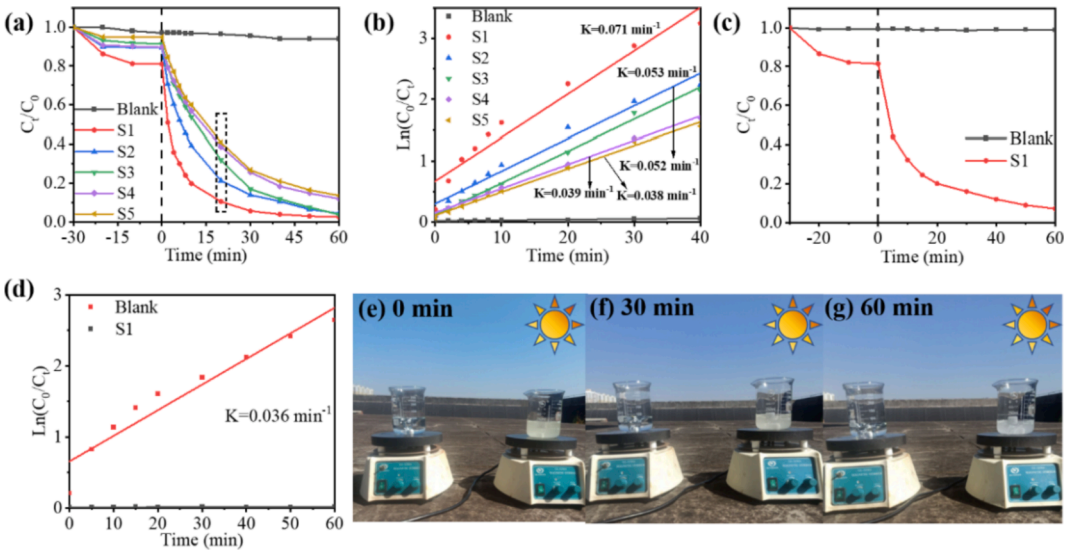

Fig. 4. (a) Photodegradation curves and (b) kinetic curves of TCH (20 mg L^{-1}, 100 mL) with different photocatalysts under UV–vis light irradiation, (c) degradation dynamic curves and (d) kinetic curves of TCH with sample S1 under actual sunlight light irradiation, and (e-g) photos of the actual outdoor TCH degradation experiment.

intensity of sample S1 were not only lower but also wider. In addition, a blue shift was observed for the peak position of sample S1, which is caused by the introduction of OVs [40].

In addition, UV–*vis* spectroscopy can be used to determine the optical properties of BiOBr samples. The Fig. S6 and Fig. 3c demonstrate the UV–*vis* diffuse reflectance spectra of the BiOBr samples. It is clear from Fig. S5d that most of the absorption edges of the samples are below 410 nm. In contrast, the absorption wavelength of sample S1 is extended to 450 nm since the existence of OV, resulting in excellent light-scattering ability of its hierarchical structure. Correspondingly, the band gap energies of the samples are calculated from Tauc's plots [41] with estimated band gaps of 2.54, 2.81 2.78, 2.10 and 2.74 eV, respectively, among which sample S1 displays a narrower band gap. Hence, the defect level will be introduced into the band gap owning to the presence of OVs to narrow the band gap [42], which promotes light absorption in visible light region and benefiting the photoactivity of sample S1.

Photoluminescence (PL) spectroscopy characterization can be used to detect the separation and transfer efficiency of charge carriers. According to the previous literature, the peak around 440 nm corresponds to the edge emission of the BiOBr intrinsic band [43]. As we know, a lower PL intensity indicates a lower recombination rate of photogenerated e^--h^+ pairs [44]. As the recombination rate decreases, the generation of active species increases and the activity will be enhanced accordingly. As shown in Fig. 3d, the sample S1 exhibits a broad emission peak. And the PL intensity in the samples follows the order of S5 > S4 > S3 > S2 > S1, which means that the recombination of photoinduced e^--h^+ pairs is effectively suppressed in the sample S1 owing to the richer content of OVs, thus improving the charge transfer efficiently. Furthermore, fluorescence lifetime measurements were used to further understand the charge carrier separation dynamics of the samples. The luminescence decay measurements were carried out at an excitation wavelength of 325 nm. The time-resolved PL decay spectra of as prepared samples are presented in Fig. S7. According to the analysis of fit curves (Table S3), the fluorescence life time τ_{av} are found to be 15.126 ns, 15.116 ns, 13.907 ns, 13.567 ns and 7.989 ns for samples S1-S5 materials, respectively. Obviously, sample S1 shows relatively prolonged life time decay than others. It also suggests that the formation of OVs in the sample can allow photogenerated electrons to be trapped by OVs before recombining with holes, leading to a slight increase in the average decay time, which is consistent with the PL analysis.

In addition, the SPV technique can provide direct information on the band gap transition of photogenerated charge carriers as the intensity represents the photogenerated carrier separation efficiency in space [45]. In Fig. 3e, it can been noted that the SPV amplitude of sample S1 is as high as about 400 μV at 350 nm, significantly stronger than those in the other catalysts, which implies that more spatially separated charges are produced in sample S1, thus exhibits the best charge separation efficiency to improve its photocatalytic degradation effect. To further understand the diffusion process of the photogenerated charge carriers, the TPV spectra of the five catalysts are shown in Fig. 3f. It can be clearly seen that all samples show the positive TPV signals, whose values increase gradually in the order of S5 < S4 < S3 < S2 < S1, implying that the photogenerated holes accumulate at the excited surface area nearby the testing electrode [46]. Moreover, the TPV signals for sample S1 have no retardation and rapidly reached their maximum, while the signals need a relatively long time to reach their maximum for sample S2-S5, indicating that sample S1 displays a slower charge mobility rate than that of the other samples. These findings are consistent with the SPV results in Fig. 3e.

3.4. Photocatalytic performance

Given to above analysis, TCH (20 mg L^{-1}) was adopted to determine the catalytic activity of the synthesized photocatalysts under UV–*vis* light irradiation (Fig. S8). As shown in 4a, the concentration of TCH of the blank line exhibits almost no change without the addition of any photocatalyst, suggesting the good photostability of TCH. While the adsorption-desorption process between TCH and photocatalysts reaches the equilibrium within 30 min in the dark which also can be proved by adsorption kinetics of TCH on sample S1 (Fig. S9 and Table. S4). Meanwhile, the adsorption capacity of sample S1 is higher than the other four samples, which may be ascribed to the richer adsorption sites from its higher surface area. Obviously, the photodegradation activity of TCH over the sample S1 is the strongest (nearly 86.8%) within the first 20 min and 96.5% degradation within 60 min, which meets the practical demand. In contrast, the TCH degradation rates are 76.1%, 64.9%, 56.7% and 56.3%, respectively for sample S2-S5 in 20 min. Meanwhile, the Fig. S10 shows the various characteristic absorption curves of TCH for the five samples corresponding to Fig. 4a. As can be calculated from the curves of $Ln(C_0/C_t)$ versus t (Fig. 4b), the corresponding rate constants k over samples S1-S5 are 0.071 min^{-1}, 0.053 min^{-1}, 0.052 min^{-1}, 0.039 min^{-1} and 0.038 min^{-1}, respectively. Accordingly, the results

indicate that sample S1 possesses greatly enhanced photocatalytic efficiency compared with other samples under UV–*vis* light irradiation. In addition, Table S5 has proved that due to the cost-effectiveness and the high degradation efficiency of TCH, the proposed BiOBr microsphere photocatalyst in this study has prominent photocatalytic activity and receives widespread application for degrading antibiotics.

To further evaluate the visible light photocatalytic response of sample S1, the similar experiment was carried out under visible light irradiation. Impressively, the TCH degradation rate of sample S1 is 70.1% in 60 min (Fig. S11a-b), while the corresponding dynamic curves (Fig. S11c) shows the k value is 0.013 min^{-1}. Although the dynamic rate has decreased, the degradation efficiency is still gratifying. Meanwhile, given to the practical application, the actual outdoor TCH degradation experiment was carried out from 12 to 13o'clock PM (Beijing Time) with the solar power of 54.0 mW cm^{-2}. The result is that the sample S1 shows excellent actual sunlight photocatalytic performance, with the degradation rate of 91.2% in 60 min (Fig. 4c-d), while the corresponding dynamic curves (Fig. S12) shows the k value increases from 0.013 to 0.036 min^{-1}, revealing that the catalytic efficiency of sample S1 is greatly improved under sunlight irradiation. The photos and the reaction solutions of the actual outdoor TCH degradation experiment can be seen in Fig. 4e-g and Fig.S13. Hence, the above results lay a foundation for its practical application.

In summary, the above series results prove that this solvent-coordination method does allow reasonable regulations of the OV concentrations in the hierarchical 3D microspheres. In addition, the rich content of OVs and the largest surface area for sample S1 can help enhance the adsorption of the target molecules on more active sites, thus improving the practical photocatalytic activity.

The stability and recyclability of catalysts are crucial to practical wastewater treatment. Therefore, the catalytic reusability of sample S1 was evaluated by performing the same measurement over five cycles under UV–*vis* light irradiation. After each cycle, the catalyst was separated by centrifugation, washed, vacuum dried and then used to the next circulating experiment. As exhibited in Fig. 5a, the activity can be maintained at a stable level after each cycle, and the removal efficiency of TCH after 5 times is still preserved above 90.0% after 60 min irradiation. Moreover, the crystal structure and morphology of sample S1 are compared by XRD, FTIR and SEM before and after 5 times reaction. Obviously, the XRD pattern (Fig. S14a) shows that the crystal structure maintains after five cycles, indicating no collapse in the special sphere-like structure. Meanwhile, Fig. S14b shows no additional impurity peak, which means that organic impurities are not adsorbed on the surface of the catalyst. To get the close observation, as shown in Fig. S14c, the sample S1 catalyst still exhibits hierarchical 3D BiOBr microsphere structure without any destruction. Meanwhile, the released concentrations of Bi and Br from sample S1 were determined by ICP and HPIC, which are shown in Table S6. Indeed, it can be seen that the release amount of Bi and Br elements after multiple recycling can be negligible compared with the initial addition amount. The above analysis shows the excellent stability of the sample S1, underlining its great potential for photodegradation of TCH.

Usually, solution pH value confers a distinct effect on the photocatalytic performance for the degradation of organic pollutants. To evaluate the influence of solution pH on photodegradation efficiency of TCH over sample S1, the pH value of the reaction system was adjusted from 2 to 10 by adding HCl or NaOH. As shown in Fig. 5b, the degradation efficiency of TCH is almost unchanged along with the different pH values, indicating the stability against pH changes for sample S1.

Active species produced during the photocatalytic reaction are significant for degrading organic pollutants, hence, the radical trapping experiment (Fig. 5c) was carried out during TCH degradation by sample S1 to detect their types. When isopropyl alcohol (IPA) was added $^{\bullet}OH$ scavenger, there was no obvious negative effect on removal efficiency of TCH under UV–*vis* light illumination, suggesting that $^{\bullet}OH$ are not the main active species. However, with the addition of benzoquinone (BQ) or Triethanolamine (TEOA) as $^{\bullet}O_2^-$ or h^+ scavenger, the removal efficiency of TCH decreases from 96.5% to 26.0% or 3.5% respectively, suggesting that $^{\bullet}O_2^-$ and h^+ are pivotal during this photocatalytic reaction. It can be concluded that the effect order of the active species over TCH removal is $h^+ > {}^{\bullet}O_2^- > {}^{\bullet}OH$. Simultaneously, the generation of the reactive oxygen species (ROS) during BiOBr samples photocatalytic process can be detected by EPR technology. For comparison, it is noted that no signal in dark can be seen for all samples. After light illumination for 5 min, the EPR spectrum of DMPO−$^{\bullet}O_2^-$ (Fig. 5d) in methanol dispersions ascribed to existence of $^{\bullet}O_2^-$, which are generated by the molecular oxygen, since they easily capture the photoelectrons on the surface OVs then negatively charged [47,48]. Meanwhile, the typical four peaks of DMPO−$^{\bullet}OH$ (Fig. 5e) adduct with an intensity ratio of 1: 2: 2: 1 are obtained in the aqueous dispersions of all the BiOBr samples, and the intensity of DMPO−$^{\bullet}OH$ for sample S1 is significantly stronger than the other four samples, which corresponds to the photocatalytic performance. The above results indicate that h^+, $^{\bullet}O_2^-$ and $^{\bullet}OH$ are produced in the BiOBr samples in the photodegradation of TCH. As is

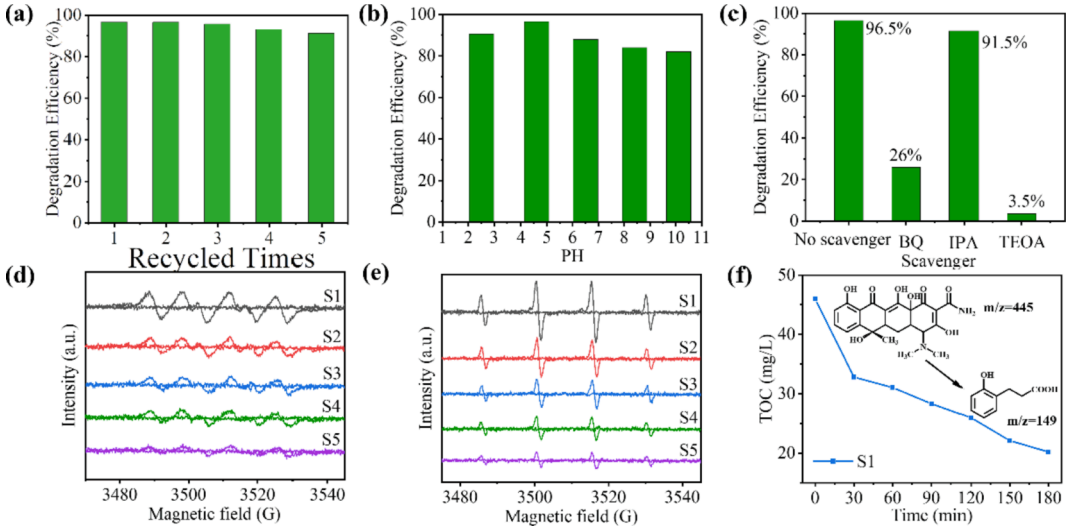

Fig. 5. (a) Cycling tests in the photodegradation of TCH by sample S1 as photocatalyst, (b) effects of solution pH on TCH degradation with sample S1, (c) the efficiencies of TCH by sample S1 without/with trapping agents; EPR spectra in methanol dispersion for (d) DMPO−$^{\bullet}O_2^-$, and in aqueous dispersion (e) DMPO−$^{\bullet}OH$; (f) the TOC concentration of TCH solution (20 mg L^{-1}, 150 mL) versus the irradiated time.

shown in Fig. 5f, it can be seen that the TOC was reduced to less than 20 mg/L by using sample S1 after 180 min irradiation, which indicates its high mineralization efficiency for TC photodegradation.

To study the degradation pathway of TC, LC-MS technique can be utilized to detect intermediates in sample S1 during the photocatalytic process. The prominent peak of initial TC at m/z = 445 (Fig. S15a) is obviously detected in the solution mass spectra, which is similar to previous studies [49,50]. Then two photocatalytic degradation pathways for the TC are proposed in Fig. 6, named A and B. For the pathway A [51], product 1 (m/z = 461) is produced through the hydration process of photogenerated $^{\bullet}OH$. Afterwards, as the ring structure breaks, products 2 (m/z = 277), 3 (m/z = 209), 6 (m/z = 149) are thus generated and the corresponding MS spectra in the UPLC-MS can be shown in Fig. S15b-d. For the pathway B [52], product 4 (m/z = 433) is generated due to the loss of an N-methyl bond as the energy of the N-C bond is reduced [53,54]. Subsequently, due to the ring break of product 1 and the $^{\bullet}OH$ radical can be oxidized to undergo a dihydroxylation reaction to produce product 5 (m/z = 301). Finally, product 5 is further oxidized to produce 6 (m/z = 149), the corresponding MS spectra in UPLC-MS are shown in Fig. S15e-g. These facts demonstrate that sample S1 can effectively degrade TCH successfully under the UV–*vis* light irradiation.

The bandgaps of perfect BiOBr and its counterpart with OVs were investigated by DFT calculations to further elucidate the mechanism of improved BiOBr photocatalytic capability, and both structures were shown in Fig. 7a and 7c. As is shown in Fig. 7b, the perfect BiOBr possesses a bandgap of 2.18 eV where all the oxygen atoms are equivalent. In the contrast, in Fig. 7d, when OVs are introduced, an occupied band at 1.1–1.2 eV above the valence band top will be produced, and the OVs shows a character of n-type doping. Hence, the DFT calculations indicates that the presence of OVs can narrow the bandgap, leading to an improved photocatalytic performance, which concretely matches the experimental findings.

3.5. Photocatalytic mechanism

We used the Mott-Schottky plot to measure the conduction band (CB) (Fig S16). Therefore, sample S1 displays a CB with the edge of the energy at about −0.05 eV. Combined with the results of optical measurements, the valence band (VB) of sample S1 is calculated to be 2.49 eV. As shown in Fig. 8, the CB potential of S1 is negative than the standard reduction potential of $O_2/^{\bullet}O_2^-$ (−0.046 eV/NHE), implying the photogenerated electrons in the CB of S1 can directly reduce dissolved O_2 to $^{\bullet}O_2^-$ [55], while the photoinduced holes leaving the VB of S1 can combine with OH^- to produce richer active $^{\bullet}OH$ due to the VB potential of S1 positive than the standard reduction potential of $OH^-/^{\bullet}OH$ (2.44 eV/NHE). Therefore, the photocatalytic activity of sample S1 are mainly attributed to the generated $^{\bullet}O_2^-$ and $^{\bullet}OH$ active species, meanwhile, parts of h^+ can also directly degrade TC.

Finally, the photodegradation mechanism based on the above viewpoints is depicted in Fig. 8. As is displayed, the diagram vividly shows the photocatalytic degradation of TC by sample S1. Firstly, TC molecules will be preferentially adsorbed by the active sites of OVs on the surface of BiOBr nanosheets, where the Br^- ions insert into the $[Bi_2O_2]^{2+}$ layers as laminated microstructures. Since large numbers of 2D ultra-thin sheet-like nanounits construct the 3D hierarchical structure with many open channels, the specific surface area is up to 57.7176 $m^2\ g^{-1}$. Such special morphology will benefit the TCH molecules adsorption, and then further facilitate the mass transportation. Secondly, the increase of OVs can help introduce more highly active reaction sites at the surface of the sample S1, enabling better excitation to generate e^- and h^+ under actual sunlight irradiation, and boost the reaction between these photo-induced e^--h^+ species and O_2, H_2O or OH^-, thus yielding more active species mentioned in Fig. 5d-e. Last but not the least, these active species (h^+, $^{\bullet}O_2^-$and $^{\bullet}OH$) have also pre-adsorbed on sample S1 catalyst and readily interact with TCH molecules, and the corresponding MS spectra of photo-degradation reaction for 30 min in the UPLC chromatogram (Fig. S17) helps to prove that the larger m/z intermediates are not available, demonstrating that TC molecules are completely degraded.

4. Conclusion

In this work, a feasible strategy was carried out to regulate the concentrations of OVs in the 3D BiOBr microsphere structure (denoted as sample S1) for photocatalytic degradation of TCH performance. Additionally, four other solvents with different polarities were also used to generate BiOBr counterparts contained various concentrations of OVs (denoted as sample S2-S5). The sample S1 with the higher content of

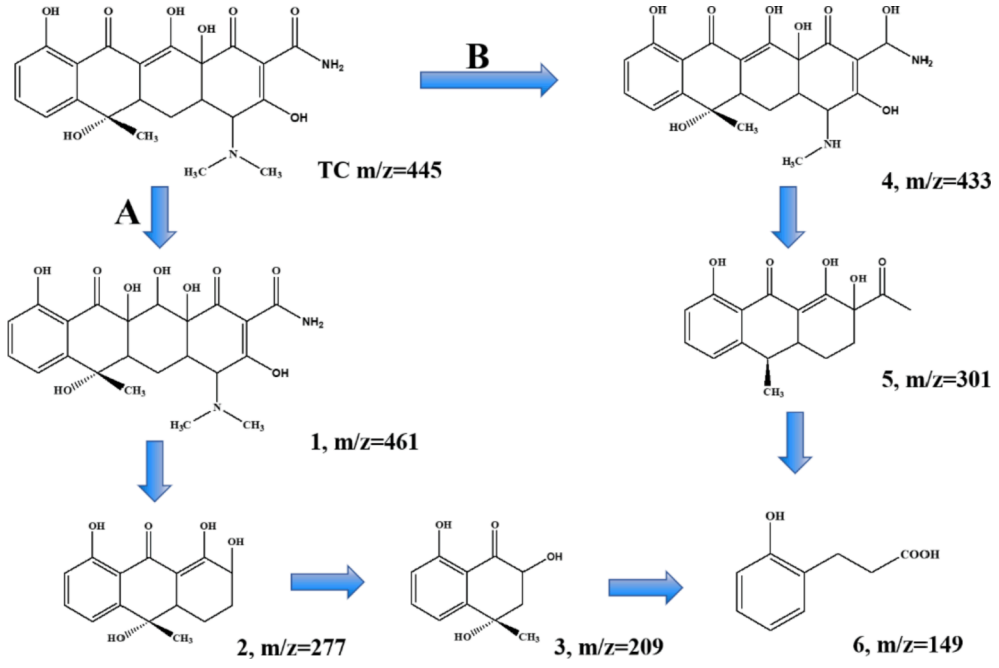

Fig. 6. The proposed photocatalytic degradation pathways of TCH under UV–*vis* light illumination in the presence of sample S1.

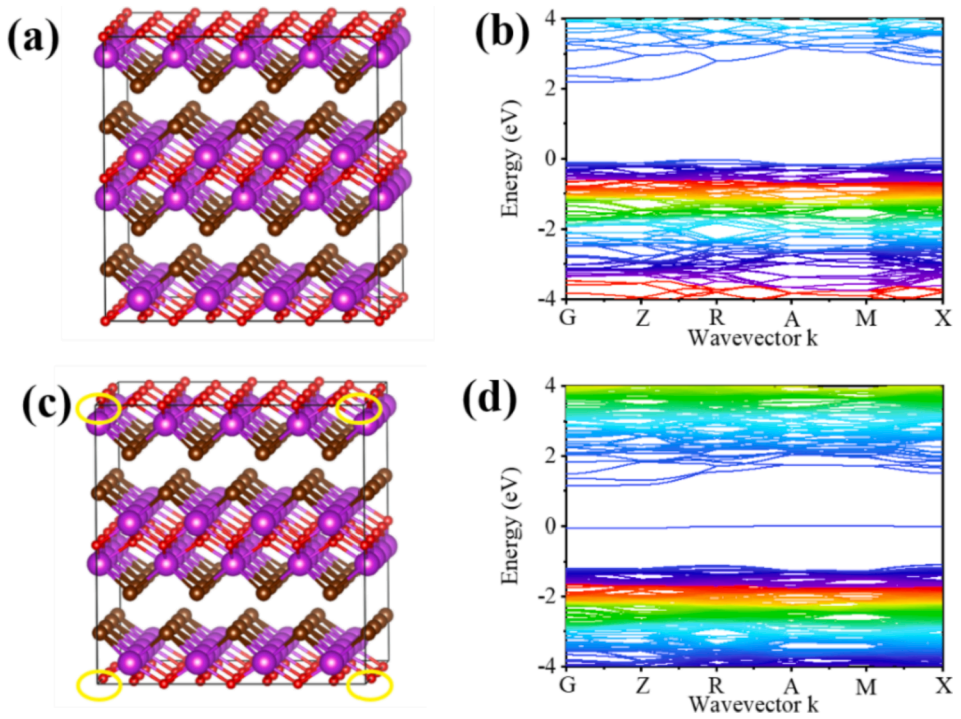

Fig. 7. (a) The structure and (b) the corresponding band structure of pure BiOBr; (c) the structure and (d) the corresponding band structure of BiOBr with OVs.

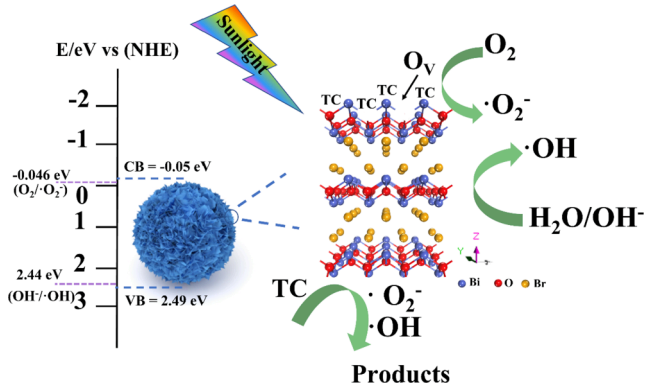

Fig. 8. Schematic illustration for the photodegradation process of TCH using sample S1 as photocatalyst.

OVs exhibits the highest degradation efficiency, with nearly 86.8% of TCH degraded within the first 20 min and 96.5% degraded within 60 min. Moreover, the photo-degradation efficiencies of sample S1 under visible light ($\lambda > 400$ nm) and actual sunlight were 70.1% and 91.2% within 60 min irradiation, respectively, which can meet the actual application. The superior photocatalytic degradation performance of sample S1 can be attributed to its rich OVs to help decrease recombination rates of e^{-}-h^{+} pairs, which is consistent with the test results of EPR, PL, SPV, TPV, etc. Furthermore, the two detailed TCH photodegradation paths were analyzed in our work via LC-MS analysis. This work not only provides new insights into the preparation of novel photocatalysts with regulated OV amount, but also presents theoretical guidance for practical photodegradation applications.

Declaration of Competing Interest

The authors declare that they have no known competing financial interests or personal relationships that could have appeared to influence the work reported in this paper.

Acknowledgments

This work was funded by the National Natural Science Foundation of China (Nos. 42030502, 42090041 and 51762005); Key Projects of Guangxi Natural Science Foundation (2020GXNSFDA297015), China; Science and Technology Major Project of Guangxi (AA18242007, AA18118030), China; Open Foundation of Guangxi Key Laboratory of Processing for Non-ferrous Metals and Featured Materials, Guangxi University (Grant No. 2020GXYSOF06), China; The Basic Scientific Research Ability Improvement Project of Young and Middle-aged Teachers in Guangxi Universities (2020KY01013), China.

Appendix A. Supplementary material

Experimental details related to materials preparation and test; **Fig. S1.** Typical SEM images of the as-prepared BiOBr samples from four different solvents: (a, b) S2 (isopropanol), (c, d) S3 (ethanol), (e, f) S4 (tetrahydrofuran), (g, h) S5 (water); **Fig. S2.** Typical TEM image of sample S1; **Fig. S3.** The EDS pattern of sample S1; **Fig. S4.** Nitrogen adsorption-desorption isotherms and the corresponding BJH pore size distribution curves of the obtained samples (inset); **Fig. S5.** (a) Survey XPS spectra, and (b-c) high-resolution XPS spectra of Bi 4f and Br 3d, (d) Raman spectra of samples S1-5 using 785 nm excitation; **Fig. S6.** UV-*vis* diffusion reflectance spectra of the as-obtained BiOBr samples; **Fig. S7.** The time-resolved photoluminescence decay curves of the five samples; **Fig. S8.** The standard curve of TCH; **Fig. S9.** Adsorption kinetics of TCH on sample S1; **Fig. S10.** (a-e) Temporal evolution of UV-*vis* spectra of TCH solution under UV-*vis* light irradiation degraded by samples S1-S5, respectively; **Fig. S11.** (a) Degradation dynamic curves, (b) time evolution of the UV-*vis* spectra and (c) kinetic profiles of sample S1 under visible light irradiation; **Fig. S12.** The time evolution of the UV-*vis* spectra of sample S1 under actual light illumination; **Fig. S13.** The reaction solutions of the actual outdoor TCH degradation experiment; **Fig. S14.** The characterizations of sample S1 before and after 5 times circular usages: (a) XRD spectra, (b) FTIR spectra and (c) SEM image; **Fig. S15.** (a-g) The corresponding MS spectra of the TC, product 1, product 2, product 3, product 4, product 5 and product 6 in the UPLC

chromatogram; **Fig. S16.** Mott-Schottky plot of sample S1; **Fig. S17.** The corresponding MS spectra of photo-degradation reaction for 30 min in the UPLC chromatogram. **Table S1.** Surface area and pore size parameters of samples S1-S5; **Table S2.** Curve fitting of O 1s in XPS spectra for samples S1-5; **Table S3.** Parameters of the time-resolved PL decay curves; **Table S4.** Adsorption kinetics parameters of TCH on sample S1; **Table S5.** Comparison of TC photodegradation with various photocatalysts; **Table S6.** The released amount of Bi and Br from sample S1 after different circles; **Supporting References.** Supplementary data to this article can be found online at https://doi.org/10.1016/j.apsusc.2022.152902.

References

[1] D.B. Wang, F.Y. Jia, H. Wang, F. Chen, Y. Fang, W.B. Dong, G.M. Zeng, X.M. Li, Q. Yang, X.Z. Yuan, Simultaneously efficient adsorption and photocatalytic degradation of tetracycline by Fe-based MOFs, J. Colloid Interface Sci. 519 (2018) 273–284, https://doi.org/10.1016/j.jcis.2018.02.067.

[2] C. Song, B.-B. Guo, X.-F. Sun, S.-G. Wang, Y.-T. Li, Enrichment and degradation of tetracycline using three-dimensional graphene/MnO_2 composites, Chem. Eng. J 358 (2019) 1139–1146, https://doi.org/10.1016/j.cej.2018.10.119.

[3] Y. Zhang, S. Zuo, Y. Zhang, G. Ren, Y. Pan, Q. Zhang, M. Zhou, Simultaneous removal of tetracycline and disinfection by a flow-through electro-peroxone process for reclamation from municipal secondary effluent, J. Hazard. Mater 368 (2019) 771–777, https://doi.org/10.1016/j.jhazmat.2019.02.005.

[4] Y. Pan, Y. Zhang, M. Zhou, J. Cai, Y. Tian, Enhanced removal of emerging contaminants using persulfate activated by UV and pre-magnetized Fe^0, Chem. Eng. J. 361 (2019) 908–918, https://doi.org/10.1016/j.cej.2018.12.135.

[5] J. Chen, X. Zhang, F. Bi, X. Zhang, Y. Yang, Y. Wang, A facile synthesis for uniform tablet-like TiO_2/C derived from Materials of Institut Lavoisier-125(Ti) (MIL-125 (Ti)) and their enhanced visible light-driven photodegradation of tetracycline, J. Colloid Interface Sci. 571 (2020) 275–284, https://doi.org/10.1016/j.jcis.2020.03.055.

[6] M. Yan, Y. Yan, Y. Wu, W. Shi, Y. Hua, Microwave-assisted synthesis of monoclinic-tetragonal $BiVO_4$ heterojunctions with enhanced visible-light-driven photocatalytic degradation of tetracycline, RSC Adv. 5 (110) (2015) 90255–90264.

[7] E.T. Helmy, E.M. Abouellef, U.A. Soliman, J.H. Pan, Novel green synthesis of S-doped TiO_2 nanoparticles using Malva parviflora plant extract and their photocatalytic, antimicrobial and antioxidant activities under sunlight illumination, Chemosphere 271 (2021) 129524, https://doi.org/10.1016/j.chemosphere.2020.129524.

[8] M. Guan, C. Xiao, J. Zhang, S. Fan, R. An, Q. Cheng, J. Xie, M. Zhou, B. Ye, Y.i. Xie, Vacancy associates promoting solar-driven photocatalytic activity of ultrathin bismuth oxychloride nanosheets, J. Am. Chem. Soc. 135 (28) (2013) 10411–10417, https://doi.org/10.1021/ja402956f.

[9] J. Li, X. Wu, W. Pan, G. Zhang, H. Chen, Vacancy-Rich Monolayer BiO_{2-x} as a Highly Efficient UV, Visible, and Near-Infrared Responsive Photocatalyst, Angew. Chem. Int. Ed. 57 (2) (2018) 491–495, https://doi.org/10.1002/anie.201708709.

[10] N. Zhang, X. Li, H. Ye, S. Chen, H. Ju, D. Liu, Y. Lin, W. Ye, C. Wang, Q. Xu, J. Zhu, L.i. Song, J. Jiang, Y. Xiong, Oxide Defect Engineering Enables to Couple Solar Energy into Oxygen Activation, J. Am. Chem. Soc. 138 (28) (2016) 8928–8935, https://doi.org/10.1021/jacs.6b04629.

[11] J.H. Pan, J. Schneider, W.Y. Teoh, Photocatalysis for environmental remediation - From laboratories to industry and beyond, Chemosphere 286 (2022) 131704, https://doi.org/10.1016/j.chemosphere.2021.131704.

[12] D. Cui, L. Wang, K. Xu, L. Ren, L.i. Wang, Y. Yu, Y.i. Du, W. Hao, Band-gap engineering of BiOCl with oxygen vacancies for efficient photooxidation properties under visible-light irradiation, J. Mater. Chem. A 6 (5) (2018) 2193–2199, https://doi.org/10.1039/C7TA09897A.

[13] F.C. Tompkins, Superficial Chemistry and Solid Imperfections, Nature 186 (4718) (1960) 3–6, https://doi.org/10.1038/186003a0.

[14] B.-Q. Li, Z.-J. Xia, B. Zhang, C. Tang, H.-F. Wang, Q. Zhang, Regulating p-block metals in perovskite nanodots for efficient electrocatalytic water oxidation, Nat. Commun. 8 (2017) 934, https://doi.org/10.1038/s41467-017-01053-x.

[15] S. Das, B. Wang, Y. Cao, M. Rae Cho, Y. Jae Shin, S. Mo Yang, L. Wang, M. Kim, S. V. Kalinin, L.Q. Chen, T.W. Noh, Controlled manipulation of oxygen vacancies using nanoscale flexoelectricity, Nat. Commun. 8 (2017) 615, https://doi.org/10.1038/s41467-017-00710-5.

[16] I. Nakamura, N. Negishi, S. Kutsuna, T. Ihara, S. Sugihara, K. Takeuchi, Role of oxygen vacancy in the plasma-treated TiO_2 photocatalyst with visible light activity for NO removal, J. Mol. Catal. A Chem. 161 (1-2) (2000) 205–212, https://doi.org/10.1016/S1381-1169(00)00362-9.

[17] L. Jing, B. Xin, F. Yuan, L. Xue, B. Wang, H. Fu, Effects of Surface Oxygen Vacancies on Photophysical and Photochemical Processes of Zn-Doped TiO_2 Nanoparticles and Their Relationships, J. Phys. Chem. B 110 (36) (2006) 17860–17865, https://doi.org/10.1021/jp063148z.

[18] M. Zhao, W. Pan, Effect of lattice defects on thermal conductivity of Ti-doped, Y_2O_3-stabilized ZrO_2, Acta Mater. 61 (14) (2013) 5496–5503, https://doi.org/10.1016/j.actamat.2013.05.038.

[19] J. Wang, P. Liu, X. Fu, Z. Li, W. Han, X. Wang, Relationship between Oxygen Defects and the Photocatalytic Property of ZnO Nanocrystals in Nafion Membranes, Langmuir 25 (2) (2009) 1218–1223, https://doi.org/10.1021/la803370z.

[20] D.B. Miklos, C. Remy, M. Jekel, K.G. Linden, J.E. Drewes, U. Hübner, Evaluation of advanced oxidation processes for water and wastewater treatment – A critical review, Water Res. 139 (2018) 118–131, https://doi.org/10.1016/j.watres.2018.03.042.

[21] C. Mao, H. Cheng, H. Tian, H. Li, W.-J. Xiao, H. Xu, J. Zhao, L. Zhang, Visible light driven selective oxidation of amines to imines with BiOCl: Does oxygen vacancy concentration matter? Appl. Catal. B 228 (2018) 87–96, https://doi.org/10.1016/j.apcatb.2018.01.018.

[22] J. Lyu, Z. Hu, Z. Li, M. Ge, Removal of tetracycline by BiOBr microspheres with oxygen vacancies: Combination of adsorption and photocatalysis, J. Phys. Chem. Solids 129 (2019) 61–70, https://doi.org/10.1016/j.jpcs.2018.12.041.

[23] J. Sun, X. Li, Q. Zhao, B. Liu, Ultrathin nanoflake-assembled hierarchical BiOBr microflower with highly exposed 001 facets for efficient photocatalytic degradation of gaseous ortho-dichlorobenzene, Appl. Catal. B 281 (2021) 119478, https://doi.org/10.1016/j.apcatb.2020.119478.

[24] X. Tong, X. Cao, T. Han, W.-C. Cheong, R. Lin, Z. Chen, D. Wang, C. Chen, Q. Peng, Y. Li, Convenient fabrication of BiOBr ultrathin nanosheets with rich oxygen vacancies for photocatalytic selective oxidation of secondary amines, Nano Res. 12 (7) (2019) 1625–1630, https://doi.org/10.1007/s12274-018-2404-x.

[25] J. Zhao, Z. Miao, Y. Zhang, G. Wen, L. Liu, X. Wang, X. Cao, B. Wang, Oxygen vacancy-rich hierarchical BiOBr hollow microspheres with dramatic CO_2 photoreduction activity, J. Colloid Interface Sci. 593 (2021) 231–243, https://doi.org/10.1016/j.jcis.2021.02.117.

[26] S. Wu, W. Sun, J. Sun, Z.D. Hood, S.-Z. Yang, L. Sun, P.R.C. Kent, M.F. Chisholm, Surface Reorganization Leads to Enhanced Photocatalytic Activity in Defective BiOCl, Chem. Mater. 30 (15) (2018) 5128–5136, https://doi.org/10.1021/acs.chemmater.8b01629.

[27] S. Yu, Y. Zhang, F. Dong, M. Li, T. Zhang, H. Huang, Readily achieving concentration-tunable oxygen vacancies in $Bi_2O_2CO_3$: Triple-functional role for efficient visible-light photocatalytic redox performance, Appl. Catal. B 226 (2018) 441–450, https://doi.org/10.1016/j.apcatb.2017.12.074.

[28] T. Kanagaraj, S. Thiripuranthagan, Photocatalytic activities of novel $SrTiO_3$-BiOBr heterojunction catalysts towards the degradation of reactive dyes, Appl. Catal. B 207 (2017) 218–232, https://doi.org/10.1016/j.apcatb.2017.01.084.

[29] Y. Wang, X. Jiang, Y. Xia, A Solution-Phase, Precursor Route to Polycrystalline SnO_2 Nanowires That Can Be Used for Gas Sensing under Ambient Conditions, Chem. Mater. 125 (52) (2003) 16176–16177, https://doi.org/10.1021/ja037743f.

[30] X. Jiang, Y. Wang, T. Herricks, Y. Xia, Ethylene Glycol-Mediated Synthesis of Metal Oxide Nanowires, J. Mater. Chem. 14 (2004) 695–703, https://doi.org/10.1039/B313938G.

[31] J. Xiong, G. Cheng, Z. Lu, J. Tang, X. Yu, R. Chen, BiOCOOH hierarchical nanostructures: Shape-controlled solvothermal synthesis and photocatalytic degradation performances, CrystEngComm 13 (2011) 2381–2390, https://doi.org/10.1039/C0CE00705F.

[32] Y. Wang, J. He, Y. Zhu, H. Zhang, C. Yang, K. Wang, S.-C. Wu, Y.-L. Chueh, W. Jiang, Hierarchical Bi-doped BiOBr microspheres assembled from nanosheets with (0 0 1) facet exposed via crystal facet engineering toward highly efficient visible light photocatalysis, Appl. Surf. Sci. 514 (2020), 145927, https://doi.org/10.1016/j.apsusc.2020.145927.

[33] H. Feng, Z. Xu, L. Ren, C. Liu, J. Zhuang, Z. Hu, X. Xu, J. Chen, J. Wang, W. Hao, Y. i. Du, S.X. Dou, Activating Titania for Efficient Electrocatalysis by Vacancy Engineering, ACS Catal. 8 (5) (2018) 4288–4293, https://doi.org/10.1021/acscatal.8b00719.

[34] X. Mu, Q. Wen, G. Ou, Y. Du, P. He, M. Zhong, H. Zhu, H. Wu, S. Yang, Y. Liu, B. Li, X. Zhang, H. Zhou, A current collector covering nanostructured villous oxygen-deficient NiO fabricated by rapid laser-scan for Li-O_2 batteries, Nano Energy 51 (2018) 83–90, https://doi.org/10.1016/j.nanoen.2018.06.043.

[35] G. Ou, Y. Xu, B. Wen, R. Lin, B. Ge, Y. Tang, Y. Liang, C. Yang, K. Huang, D. Zu, R. Yu, W. Chen, J. Li, H. Wu, L.-M. Liu, Y. Li, Tuning defects in oxides at room temperature by lithium reduction, Nat. Commun. 9 (2018) 1302, https://doi.org/10.1038/s41467-018-03765-0.

[36] X. Chen, X.u. Zhang, Y.-H. Li, M.-Y. Qi, J.-Y. Li, Z.-R. Tang, Z. Zhou, Y.-J. Xu, Transition metal doping BiOBr nanosheets with oxygen vacancy and exposed 102 facets for visible light nitrogen fixation, Appl. Catal. B 281 (2021) 119516, https://doi.org/10.1016/j.apcatb.2020.119516.

[37] Z. He, Y. Shi, C. Gao, L. Wen, J. Chen, S. Song, BiOCl/$BiVO_4$ p–n Heterojunction with Enhanced Photocatalytic Activity under Visible-Light Irradiation, J. Phys. Chem. C 118 (1) (2014) 389–398, https://doi.org/10.1021/jp409598s.

[38] L. Han, Y. Guo, Z. Lin, H. Huang, 0D to 3D controllable nanostructures of BiOBr via a facile and fast room-temperature strategy, Colloids Surf. A Physicochem. Eng. Asp. 603 (2020) 125233, https://doi.org/10.1016/j.colsurfa.2020.125233.

[39] D. Wu, B.o. Wang, W. Wang, T. An, G. Li, T.W. Ng, H.Y. Yip, C. Xiong, H.K. Lee, P. K. Wong, Visible-light-driven BiOBr nanosheets for highly facet-dependent photocatalytic inactivation of Escherichia coli, J. Mater. Chem. A 3 (29) (2015) 15148–15155, https://doi.org/10.1039/C5TA02757H.

[40] H. Li, J. Shi, K. Zhao, L. Zhang, Sustainable molecular oxygen activation with oxygen vacancies on the 001 facets of BiOCl nanosheets under solar light, Nanoscale 6 (23) (2014) 14168–14173, https://doi.org/10.1039/C4NR04810E.

[41] W. Xu, Z. Liu, A.C. Johnston-Peck, S.D. Senanayake, G. Zhou, D. Stacchiola, E. A. Stach, J.A. Rodriguez, Steam Reforming of Ethanol on Ni/CeO_2: Reaction Pathway and Interaction between Ni and the CeO_2 Support, ACS Catal. 3 (5) (2013) 975–984, https://doi.org/10.1021/cs4000969.

[42] L.-Y. Lin, S. Kavadiya, X. He, W.-N. Wang, B.B. Karakocak, Y.-C. Lin, M.Y. Berezin, P. Biswas, Engineering stable Pt nanoparticles and oxygen vacancies on defective TiO_2 via introducing strong electronic metal-support interaction for efficient CO_2

photoreduction, Chem. Eng. J. 389 (2020) 123450, https://doi.org/10.1016/j.cej.2019.123450.
[43] H. Wang, D. Yong, S. Chen, S. Jiang, X. Zhang, W. Shao, Q. Zhang, W. Yan, B. Pan, Y.i. Xie, Oxygen-Vacancy-Mediated Exciton Dissociation in BiOBr for Boosting Charge-Carrier-Involved Molecular Oxygen Activation, J. Am. Chem. Soc. 140 (5) (2018) 1760–1766, https://doi.org/10.1021/jacs.7b10997.
[44] L. Ye, X. Jin, C. Liu, C. Ding, H. Xie, K.H. Chu, P.K. Wong, Thickness-ultrathin and bismuth-rich strategies for BiOBr to enhance photoreduction of CO_2 into solar fuels, Appl. Catal. B 187 (2016) 281–290, https://doi.org/10.1016/j.apcatb.2016.01.044.
[45] S.-S. Yi, B.-R. Wulan, J.-M. Yan, Q. Jiang, Highly Efficient Photoelectrochemical Water Splitting: Surface Modification of Cobalt-Phosphate-Loaded Co_3O_4/Fe_2O_3 p–n Heterojunction Nanorod Arrays, Adv. Funct. Mater. 29 (11) (2019) 1801902, https://doi.org/10.1002/adfm.201801902.
[46] X. Wei, T. Xie, L. Peng, W. Fu, J. Chen, Q. Gao, G. Hong, D. Wang, Effect of Heterojunction on the Behavior of Photogenerated Charges in $Fe_3O_4@Fe_2O_3$ Nanoparticle Photocatalysts, J. Phys. Chem. C 115 (17) (2011) 8637–8642, https://doi.org/10.1021/jp111250z.
[47] H. Ji, L. Lyu, L. Zhang, X. An, C. Hu, Oxygen vacancy enhanced photostability and activity of plasmon-Ag composites in the visible to near-infrared region for water purification, Appl. Catal. B 199 (2016) 230–240, https://doi.org/10.1016/j.apcatb.2016.06.037.
[48] H. Li, J. Li, Z. Ai, F. Jia, L. Zhang, Oxygen Vacancy-Mediated Photocatalysis of BiOCl: Reactivity, Selectivity, and Perspectives, Angew. Chem. Int. Ed. 57 (1) (2018) 122–138, https://doi.org/10.1002/anie.201705628.
[49] Z. Zhu, P. Huo, Z. Lu, Y. Yan, Z. Liu, W. Shi, C. Li, H. Dong, Fabrication of magnetically recoverable photocatalysts using g-C_3N_4 for effective separation of charge carriers through like-Z-scheme mechanism with Fe_3O_4 mediator, Chem. Eng. J. 331 (2018) 615–625, https://doi.org/10.1016/j.cej.2017.08.131.
[50] D. Jiang, T. Wang, Q. Xu, D. Li, S. Meng, M. Chen, Perovskite oxide ultrathin nanosheets/g-C_3N_4 2D–2D heterojunction photocatalysts with significantly enhanced photocatalytic activity towards the photodegradation of tetracycline, Appl. Catal. B 201 (2017) 617–628, https://doi.org/10.1016/j.apcatb.2016.09.001.
[51] Z. Shi, Y. Zhang, X. Shen, G. Duoerkun, B.o. Zhu, L. Zhang, M. Li, Z. Chen, Fabrication of g-C_3N_4/BiOBr heterojunctions on carbon fibers as weaveable photocatalyst for degrading tetracycline hydrochloride under visible light, Chem. Eng. J. 386 (2020) 124010, https://doi.org/10.1016/j.cej.2020.124010.
[52] M. Cao, P. Wang, Y. Ao, C. Wang, J. Hou, J. Qian, Visible light activated photocatalytic degradation of tetracycline by a magnetically separable composite photocatalyst: Graphene oxide/magnetite/cerium-doped titania, J. Colloid Interface Sci. 467 (2016) 129–139, https://doi.org/10.1016/j.jcis.2016.01.005.
[53] Y. Yan, S. Sun, Y. Song, X. Yan, W. Guan, X. Liu, W. Shi, Microwave-assisted in situ synthesis of reduced graphene oxide-$BiVO_4$ composite photocatalysts and their enhanced photocatalytic performance for the degradation of ciprofloxacin, J. Hazard. Mater. 250–251 (2013) 106–114, https://doi.org/10.1016/j.jhazmat.2013.01.051.
[54] S. Jiao, S. Zheng, D. Yin, L. Wang, L. Chen, Aqueous photolysis of tetracycline and toxicity of photolytic products to luminescent bacteria, Chemosphere 73 (3) (2008) 377–382, https://doi.org/10.1016/j.chemosphere.2008.05.042.
[55] N.a. Tian, H. Huang, Y. He, Y. Guo, T. Zhang, Y. Zhang, Mediator-free direct Z-scheme photocatalytic system: $BiVO_4$/g-C_3N_4 organic–inorganic hybrid photocatalyst with highly efficient visible-light-induced photocatalytic activity, Dalton Trans. 44 (9) (2015) 4297–4307, https://doi.org/10.1039/C4DT03905J.